

The evolution of C₄H and *c*-C₃H₂ in molecular cores

Yijia Liu^{1,2}, Jun Zhi Wang^{1,*}, Ningyu Tang², Yang Lu³, Donghui Quan⁴, Juan Li⁵, Kai Yang^{6,7}, Shu Liu⁸, Yuqiang Li⁹, Siqi Zheng^{5,10,11}, and Chao Ou¹

¹ Guangxi Key Laboratory for Relativistic Astrophysics, School of Physical Science and Technology, Guangxi University, Nanning 530004, PR China

² Department of Physics, Anhui Normal University, Wuhu, Anhui 241002, PR China

³ Research Center for Computational Earth and Space Science, Zhejiang Laboratory, Hangzhou 311100, China

⁴ Department of Physics, Xi'an Jiaotong-Liverpool University, 111 Ren'ai Road, Dushu Lake Science and Education Innovation District, Suzhou 215123, Jiangsu Province, People's Republic of China

⁵ State Key Laboratory of Radio Astronomy and Technology, Shanghai Astronomical Observatory, Chinese Academy of Sciences, 80 Nandan Road, Shanghai 200030, China

⁶ Department of Astronomy, School of Physics and Astronomy, and Shanghai Key Laboratory for Particle Physics and Cosmology, Shanghai Jiao Tong University, Shanghai 200240, People's Republic of China

⁷ State Key Laboratory of Dark Matter Physics, Shanghai Jiao Tong University, Shanghai 200240, People's Republic of China

⁸ National Astronomical Observatories, Chinese Academy of Sciences, Beijing 100101, People's Republic of China

⁹ Korea Astronomy and Space Science Institute, No. 776, Daedeok-daero, Yuseong-gu, Daejeon, Republic of Korea

¹⁰ I. Physikalisches Institut, Universität zu Köln, Zùlpicher Str. 77, 50937 Köln, Germany

¹¹ School of Astronomy and Space Sciences, University of Chinese Academy of Sciences, No. 19A Yuquan Road, Beijing 100049, People's Republic of China

Received xx; accepted xxx

ABSTRACT

Context. Linear C₄H and cyclic *c*-C₃H₂, as small unsaturated hydrocarbons, are the key precursors to complex organic molecules and are critical components of the interstellar medium. However, observational constraints on the evolution of these molecules in late-stage massive star-forming regions remain scarce.

Aims. We present on-the-fly mapping observations of C₄H 9–8 lines, *c*-C₃H₂ 2–1, H¹³CO⁺ 1–0, and H42 α toward a sample of 22 massive star-forming regions using the IRAM 30m telescope. Our aim is to further explore the evolution of these carbon-chain molecules by combining observational results obtained in cold cores.

Methods. We employed H¹³CO⁺ 1–0 and H42 α as tracers to probe the positions of molecular cloud cores and ionised hydrogen regions (H II regions), respectively. One chemical model in particular, which includes gas, dust grain surface, and icy mantle phases for C₄H and *c*-C₃H₂ molecules, was used to make comparisons with observed abundances.

Results. From mapping observations targeting 31 regions across 22 sources, C₄H 9–8 ($J = 19/2-17/2$) and C₄H 9–8 ($J = 17/2-15/2$) were detected in only 17 regions, while H¹³CO⁺ 1–0 and *c*-C₃H₂ 2–1 were successfully detected in all 31 regions. We find that the emission of C₄H 9–8 and *c*-C₃H₂ 2–1 is concentrated at the edges of H42 α emission regions. The C₄H/H¹³CO⁺ and *c*-C₃H₂/H¹³CO⁺ relative abundance ratios range from 0.17 to 1.77 (median ~ 0.57) and 1.42 to 6.69 (median ~ 4.19), respectively, with a median C₄H/*c*-C₃H₂ ratio of 0.13. By combining the observational results of cold cores, we find that C₄H/H¹³CO⁺ and *c*-C₃H₂/H¹³CO⁺ ratios show a strong decreasing trend as molecular cores evolve.

Conclusions. The decreasing trends in C₄H/H¹³CO⁺ and *c*-C₃H₂/H¹³CO⁺ ratios imply that small unsaturated hydrocarbons can be consumed and converted into other organic molecules during the evolution of molecular cores. The spatial concentration of C₄H and *c*-C₃H₂ emission at the edges of H42 α regions further supports their role as precursors in the chemical pathways that lead to complex organic molecules in the interstellar medium.

Key words. ISM: clouds – ISM: molecules – ISM: abundances – ISM: evolution

1. Introduction

The interstellar medium harbours a rich diversity of carbon-bearing molecules. Among these, unsaturated hydrocarbon molecules play a pivotal role in tracing chemical evolution, with small unsaturated hydrocarbons such as C₄H and *c*-C₃H₂ serving as crucial fundamental building blocks for the formation of more complex organic molecules. The evolution of unsaturated organic molecules in molecular clouds is critically important, as it represents a crucial stellar feedback mechanism that provides essential constraints for understanding star formation processes

(Awad & Viti 2022). Regarding C₄H and *c*-C₃H₂, strong emission has been detected in TMC-1 (Irvine et al. 1981; Thaddeus et al. 1985; Madden et al. 1989), the starless core L1521F (Harada & Herbst 2008; Takakuwa et al. 2011), and the cold molecular cores (Liu et al. 2024), where their relative abundances are relatively high. However, studies examining the evolution of carbon-chain molecules in massive star-forming regions are still relatively limited.

C₄H, a prototypical linear carbon chain molecule, is predominantly formed via gas-phase processes and exists primarily as a gas-phase species. Drawing on several astrochemical networks, C₄H can be formed by some routes for the C_{*n*}H fam-

* Corresponding author; junzhiwang@gxu.edu.cn

ily and through $C + C_3H_2 \rightarrow C_4H + H$ (Loison et al. 2014; Remijan et al. 2023). The destruction of C_4H is dominated by the reaction with oxygen, $C_4H + O \rightarrow CO + C_3H$ (Loison et al. 2014), and through the radiative association of an electron, a process that disrupts its molecular structure and forms C_4H^- (Harada & Herbst 2008; Gianturco et al. 2016). The cyclic isomer $c\text{-}C_3H_2$ is observed to be comparatively abundant relative to its linear counterparts $l\text{-}C_3H_2$ within the interstellar medium. It forms in the gas phase via dissociative recombination of $C_3H_3^+ + e^- \rightarrow c\text{-}C_3H_2 + H$ (Fossé et al. 2001) and isomerisation of $l\text{-}C_3H_2$ ($H + l\text{-}C_3H_2 \rightarrow H + c\text{-}C_3H_2$) (Loison et al. 2017). The primary destruction pathway of $c\text{-}C_3H_2$ corresponds to the gas-phase reaction with atomic oxygen (O), HC_3O , and other oxygen-bearing fragments, while its reaction with C atoms facilitates carbon-chain growth to form molecules such as C_4H (Loison et al. 2017). This reaction exhibits high efficiency at low temperatures.

Liu et al. (2024) found distinct spatial distributions of C_4H 9–8 and $c\text{-}C_3H_2$ 2–1 across 19 Galactic cold cores in the early stages of star formation. Furthermore, it was found that C_4H and $c\text{-}C_3H_2$ may not have a tight chemical link in cold molecular cores and their abundances relative to H_2 are approximately 10^{-9} (Liu et al. 2024). The abundance of these two unsaturated hydrocarbon molecules (C_4H and $c\text{-}C_3H_2$) is likely to decrease as the molecular cloud evolves. Consistent with this trend, a survey conducted with the Yebes 40-m telescope by Taniguchi et al. (2024) revealed that C_4H and $c\text{-}C_3H_2$ were detected in the majority of 11 intermediate-mass cores, with their abundances being lower than those observed in the low-mass protostar L1527. In a survey of diffuse and marginally translucent clouds toward compact extragalactic millimeter-continuum sources, Lucas & Liszt (2000) also detected the hydrocarbons C_4H and $c\text{-}C_3H_2$ within these extragalactic sources. However, current studies on such unsaturated hydrocarbons in late-stage massive star-forming regions remain scarce. To gain deeper insights into the evolution of C_4H and $c\text{-}C_3H_2$ in star-forming regions at different evolutionary stages, mapping observations in the massive star-forming regions are necessary.

In this paper, we present mapping observations of C_4H 9–8 lines, $c\text{-}C_3H_2$ 2–1, $H^{13}CO^+$ 1–0, and $H42\alpha$ toward a relatively large sample of 22 Galactic late-stage massive star-forming regions with known 6.7 GHz CH_3OH masers using the Institut de Radioastronomie Millimétrique (IRAM) 30-meter telescope. We investigate the spatial distributions and relative abundances of C_4H and $c\text{-}C_3H_2$ in these regions to better understand the evolution of carbon-chain molecules. The observations and data reduction are described in Sect. 2, and the results in Sect. 3. A discussion is presented in Sect. 4 and a brief summary in Sect. 5.

2. Observation and data reduction

The 22 targets, selected from Reid et al. (2014), are late-stage massive star-forming regions with 6.7 GHz CH_3OH masers, for which accurate trigonometric parallaxes have been measured. On-the-fly (OTF) mapping observations were carried out using the IRAM 30-meter telescope, located at Pico Veleta, Spain, during July 2019, October 2019, November 2019, December 2020, and January 2021. The observational data were acquired using the Eight Mixer Receiver (EMIR) operating 3 mm (E0) band, coupled with the Fourier Transform Spectrometers (FTS) backend, which provided an instantaneous bandwidth of 8 GHz. The system delivered a spectral resolution of 195 kHz with dual polarisation capability. The IRAM 30 m telescope has a beam size of $\sim 24''$ at 85 GHz. A pixel size of $9''$ was adopted for re-

gridding of the OTF data. The system temperatures remained stable at approximately 150 K. The telescope pointing accuracy was maintained through regular calibration every ~ 2 hours using strong nearby quasi-stellar objects as reference points. The focus was calibrated prior to each observation, as well as at sunrise and sunset.

The main beam brightness temperature (T_{mb}) was derived by $T_{mb} = T_A^* \cdot F_{eff}/B_{eff}$, where T_A^* represents the antenna temperature. For the 3 mm band observations, the forward efficiency, F_{eff} , and beam efficiency, B_{eff} , were 0.95 and 0.81, respectively. The following molecular lines within the observed frequency range were analysed in this study: C_4H 9–8 (85.634.0044 MHz, $J=19/2-17/2$; 85634.0154 MHz, $J=19/2-19/2$; 85672.5793 MHz, $J=17/2-15/2$; 85672.5815 MHz, $J=17/2-17/2$), $c\text{-}C_3H_2$ 2–1 (85338.8940 MHz), $H^{13}CO^+$ 1–0 (86754.2884 MHz), and $H42\alpha$ at 85688.4 MHz. Owing to significant line blending, C_4H 9–8 ($J = 19/2-17/2$) and C_4H 9–8 ($J = 19/2-19/2$) are treated as a single feature and denoted as C_4H 9–8 ($J = 19/2-17/2$) in this work. An analogous approach was applied to the C_4H 9–8 ($J = 17/2-15/2$) and C_4H 9–8 ($J = 17/2-17/2$) transitions. The parameters for the molecular lines were extracted from the Cologne Database for Molecular Spectroscopy (CDMS¹; Müller et al. 2005) and summarised in Table 1.

The data reduction was performed using the GILDAS software package², specifically employing the CLASS and GREG applications. For each molecular line detected in the observed sources, we first determined the velocity range of the spectral emission features. Following the removal of a first-order baseline, these velocity ranges were utilised as a mask and setup window within the CLASS software. The spatial distribution of each line was obtained by applying the print area function in CLASS to extract velocity-integrated flux maps at each spatial pixel.

3. Results

From the mapping observations, multiple emission peaks were detected in several sources. Thus, a total of 31 regions were selected across 22 sources. C_4H (9–8, $J = 19/2-17/2$) and C_4H (9–8, $J = 17/2-15/2$) were detected in only 17 regions, while $H^{13}CO^+$ (1–0) and $c\text{-}C_3H_2$ (2–1) were successfully detected in all 31 regions. The detailed detection results of these molecular lines are summarised in Table B.2.

3.1. Spatial distribution of C_4H , $c\text{-}C_3H_2$, and $H^{13}CO^+$ lines

Given the relatively weak individual signals of C_4H 9–8 ($J=19/2-17/2$) and C_4H 9–8 ($J=17/2-15/2$), and considering their nearly identical Einstein coefficients and upper energy levels, it is reasonable to combine them into a single total velocity-integrated intensity. This approach provides a more reliable representation of the spatial distribution of C_4H compared to analyzing each line independently. Hereafter, C_4H 9–8 is used to represent the total velocity-integrated fluxes of C_4H 9–8 ($J=19/2-17/2$) and C_4H 9–8 ($J=17/2-15/2$).

To better demonstrate the spatial distribution of these molecular lines, two velocity-integrated intensity maps were drawn for each source. An example of the G015.03–00.67 source is shown in Fig. 1, the velocity-integrated intensity distributions of C_4H 9–8 (red contours) and $c\text{-}C_3H_2$ 2–1 (blue contours and grey scale) are presented in Fig. 1a, while the spatial distributions of $H^{13}CO^+$ 1–0 (black contours and grey scale) and $H42\alpha$ (magenta

¹ <https://cdms.astro.uni-koeln.de/classic>

² <http://www.iram.fr/IRAMFR/GILDAS>

Table 1. Physical parameters of C₄H, *c*-C₃H₂ and H¹³CO⁺ lines.

Molecular	Transition	Q _{37.50}	freq (MHz)	E_{up} (K)	g_u	A (10 ⁻⁵ s ⁻¹)
C ₄ H	N=9–8 J=19/2–17/2	660.0312	85634.0044	20.561	19	1.5175
	N=9–8 J=19/2–19/2	660.0312	85634.0154	20.561	21	1.5267
	N=9–8 J=17/2–15/2	660.0312	85672.5793	20.563	17	1.5078
	N=9–8 J=17/2–17/2	660.0312	85672.5815	20.563	19	1.5193
<i>c</i> -C ₃ H ₂	J=2(1,2)–1(0,1)	566.8560	85338.8940	6.445	15	2.3221
H ¹³ CO ⁺	J=1–0	18.3516	86754.2884	4.164	3	3.8535

contours) are illustrated in Fig. 1b. The remaining spatial distribution maps are illustrated in Appendix A.1 and the parameter settings for the maps of molecular emission lines in each source are summarised in Table B.3.

Among the eight sources for which spatial distribution maps of C₄H 9–8 were obtained, six sources exhibited clear and well-defined spatial structures. However, due to limitations in sensitivity and spatial resolution, the maps of C₄H 9–8 could not be resolved in the sources G034.39+00.22 and G075.76+00.33. In all sources where the *c*-C₃H₂ 2–1 (22 sources), H¹³CO⁺ 1–0 (22 sources), and H42 α (9 sources) were detected, we identified significant and well-resolved spatial distribution structures. The detailed spatial distribution information of C₄H 9–8, *c*-C₃H₂ 2–1, H¹³CO⁺ 1–0, and H42 α lines is presented in Table B.4.

Six of the eight sources detected in C₄H 9–8 exhibit spatial distribution structures that differ significantly from those of *c*-C₃H₂ 2–1 and H¹³CO⁺ 1–0. Despite the fact that the emission of C₄H 9–8 is relatively weak in both G034.39+00.22 and G075.76+00.33, the emission peaks are not found to be significantly different from *c*-C₃H₂ 2–1 and H¹³CO⁺ 1–0. Furthermore, H42 α was detected in four of these eight sources, with the spatial structures of three sources exhibiting significant differences, except for G075.76+00.33.

In 14 of the 22 sources where *c*-C₃H₂ 2–1 was detected (G005.88–00.39, G011.91–00.61, G015.03–00.67, G023.43–00.18, G031.28+00.66, G034.39+00.22, G035.19–00.74, G035.19–01.74, G037.43+01.51, G075.76+00.33, G081.19+01.51, G081.75+00.59, G081.87+00.78, and G121.29+00.65), the spatial distribution of *c*-C₃H₂ 2–1 was not found to differ from that of H¹³CO⁺ 1–0. In contrast, the remaining eight sources (G012.80–00.20, G043.16+00.01, G049.48–00.36, G049.48–00.38, G109.87+02.11, G111.54+00.77, G133.94+01.06, and G192.60–00.04) exhibited significantly different spatial structures between *c*-C₃H₂ 2–1 and H¹³CO⁺ 1–0. In the sources G012.80–00.20, G043.16+00.01, G049.48–00.36, G049.48–00.38, and G109.87+02.11, the spatial distribution differences between *c*-C₃H₂ 2–1 and H¹³CO⁺ 1–0 are primarily characterised by the significantly weaker emission of *c*-C₃H₂ 2–1 at the peak excitation regions of H¹³CO⁺ 1–0. This observed discrepancy suggests that *c*-C₃H₂ 2–1 may have been depleted or consumed during the process of stellar evolution in these regions, while all nine sources in which H42 α was detected with *c*-C₃H₂ 2–1 showed a clearly different spatial distribution. The individual sources providing useful spatial information are annotated below.

G015.03-00.67: The mapping size of C₄H 9–8, *c*-C₃H₂ 2–1, H¹³CO⁺ 1–0, and H42 α is 240'' \times 240''. Strong emissions of C₄H 9–8, *c*-C₃H₂ 2–1, H¹³CO⁺ 1–0, and H42 α were detected, each exhibiting a distinct and well-resolved spatial structure. The emission peaks of *c*-C₃H₂ 2–1 and H¹³CO⁺ 1–0 locate at approximately (10'', 40'') of the map, with no significant spatial

differences. Both transitions display an extended spatial distribution, covering a region of about 180'' \times 240'', and they are primarily concentrated along the edges of the H42 α emission. In contrast, the C₄H 9–8 emission is fragmented and lies primarily along the eastern edge of *c*-C₃H₂ 2–1 region. Meanwhile, the H42 α emission forms a band-like structure predominantly along the south-eastern part of the source G015.03-00.67. Its emission peak lies near (45'', 40''), slightly offset from those of *c*-C₃H₂ 2–1 and H¹³CO⁺ 1–0.

G023.43-00.18: The OTF mode was used to cover 120'' \times 120'' for C₄H 9–8, *c*-C₃H₂ 2–1, H¹³CO⁺ 1–0, and H42 α . All these lines, except for H42 α , were successfully detected. C₄H 9–8 and *c*-C₃H₂ 2–1 exhibit different spatial distributions. The C₄H 9–8 emission is primarily concentrated at south of the *c*-C₃H₂ 2–1, with a slight offset between their peak positions, approximately centered at (-10'', 10'') and (0'', -10''), respectively. In contrast, no significant spatial differences were observed between the distributions of *c*-C₃H₂ 2–1, and H¹³CO⁺ 1–0.

G049.48-00.36: A 120'' \times 120'' map of C₄H 9–8, *c*-C₃H₂ 2–1, H¹³CO⁺ 1–0, and H42 α was obtained. Although all lines were detected, C₄H 9–8 and *c*-C₃H₂ 2–1 exhibit markedly different spatial distributions, with partial overlap observed in the south-western region of *c*-C₃H₂ 2–1 emission. *c*-C₃H₂ 2–1 emission extends across nearly the entire source, displaying two prominent peaks at approximately (40'', -20'') and (-40'', -10''). In comparison, C₄H 9–8 is primarily distributed in the southern and south-western parts of G049.48-00.36, with its peak around (-35'', -15''), closely coincides with one of the peak positions of *c*-C₃H₂ 2–1. Meanwhile, the H42 α emission is localised to the south-eastern region of G049.48-00.36, exhibiting two prominent excitation peaks at (0'', 0'') and (30'', -30'').

G049.48-00.38: The mapping size of C₄H 9–8, *c*-C₃H₂ 2–1, H¹³CO⁺ 1–0, and H42 α is 120'' \times 120''. The source is located adjacent to G049.48-00.36. All the lines were detected, though with varying characteristics. The weak C₄H 9–8 emission presents spatially unresolved due to sensitivity and spatial resolution limitations, with only a marginal detection in the south-eastern region of G049.48-00.38. In contrast, the strong *c*-C₃H₂ 2–1, H¹³CO⁺ 1–0, and H42 α emission were clearly observed, extending from the north-west to the south-east across the source.

G081.75+00.59: In this study, we divided the source G081.75+00.59 into two parts, designated as G081.75+00.59-1 and G081.75+00.59-2, with a detailed analysis of each provided separately. For both parts, the observational sizes of C₄H 9–8, *c*-C₃H₂ 2–1, H¹³CO⁺ 1–0, and H42 α are 120'' \times 120'' and 80'' \times 80'', respectively. In this source, all the molecular lines were detected, except H42 α . They exhibit extended filamentary structures spanning more than 120'', revealing distinct and resolved spatial distributions.

G192.60-00.04: The mapping size of C₄H 9–8, *c*-C₃H₂ 2–1, H¹³CO⁺ 1–0, and H42 α is 120'' \times 240''. All targeted lines have

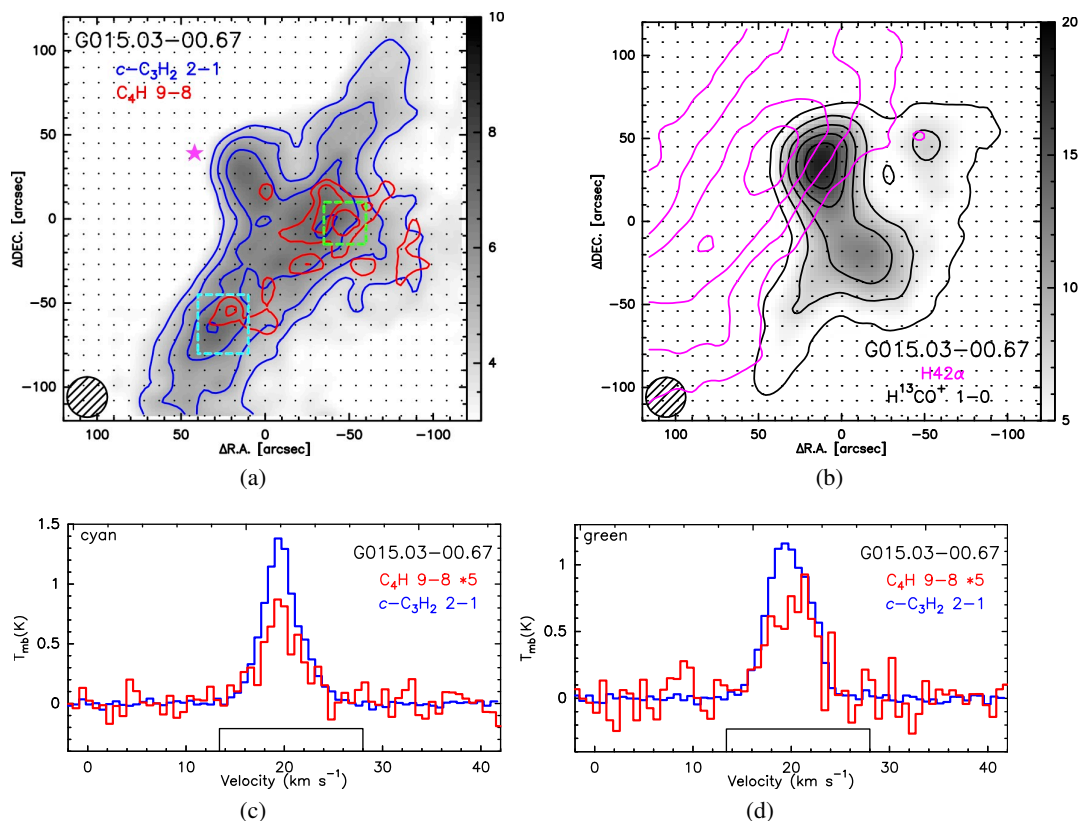


Fig. 1. Velocity-integrated intensity maps and spatial averaged spectra of C_4H 9–8, $c\text{-}C_3H_2$ 2–1, $H^{13}CO^+$ 1–0, and $H42\alpha$. The source names are presented in the maps and spectra. The grey scale colour at the right is in units of $K\ km\ s^{-1}$. (a) and (b) Velocity-integrated intensity maps of G015.03–00.67, where panel (a) shows C_4H 9–8 (red contours) overlaid on $c\text{-}C_3H_2$ 2–1 (blue contours and grey scale) and panel (b) shows $H42\alpha$ (magenta contours) overlaid on $H^{13}CO^+$ 1–0 (black contours and grey scale). The excitation peak of $H42\alpha$ is marked with a magenta five-pointed star in panel (a), (c), and (d) Spectra of C_4H at 85672.5793 MHz and $c\text{-}C_3H_2$ at 85338.8940 MHz in the green and cyan box of G015.03–00.67. The detailed mapping information of all sources for C_4H 9–8, $c\text{-}C_3H_2$ 2–1 and $H^{13}CO^+$ 1–0 are listed in Table B.3.

been detected, revealing distinct spatial distributions, except for $H42\alpha$. $H^{13}CO^+$ 1–0 emission extends from the north-west to the south-east over a region exceeding $200''$, with its peak located at $(-15'', 40'')$. In contrast, the spatial distribution of C_4H 9–8 consists of two distinct components: one component is slightly offset from the emission center of $c\text{-}C_3H_2$ 2–1, peaking at $(-10'', 30'')$, while the other lies at $(-30'', -60'')$ near the south-western edge of $c\text{-}C_3H_2$ 2–1 emission.

3.2. Column densities and relative abundances

Based on the spatial distributions of C_4H 9–8, $c\text{-}C_3H_2$ 2–1, and $H^{13}CO^+$ 1–0 in Sect. 3.1, we selected the regions with the strongest emission from each source. Since multiple emission peaks were detected in several sources, a total of 31 distinct regions were selected from 22 sources to calculate the column densities and relative abundances of the three molecules. The regions for extracting the spatially averaged spectra are marked with green dashed boxes. For maps with multiple selected regions, the second region is highlighted with a cyan box for clear distinction. The velocity-integrated intensities of these three lines were derived from the spatially averaged spectra via single-component Gaussian fitting. G049.48–00.36 and its adjacent counterpart G049.48–00.38 are both complex regions and major massive protocluster candidates in W51 (Ginsburg et al. 2012). Due to the absorption of molecular lines toward free-free continuum emission, we selected regions away from $H42\alpha$ when calculating abundances.

Next, $c\text{-}C_3H_2$ 2–1 and $H^{13}CO^+$ 1–0 emissions were detected in all 31 selected regions. Among these, C_4H 9–8 transitions (including $J=19/2\text{-}17/2$ and $J=17/2\text{-}15/2$) were detected in 17 regions, specifically: G015.03–00.67 (green and cyan), G023.43–00.18 (green), G034.39+00.22 (green), G049.48–00.36 (green and cyan), G049.48–00.38 (green and cyan), G075.76+00.33 (green), G081.75+00.59-1 (green and cyan), G081.75+00.59-2 (green and cyan), G081.87+00.78 (green), G133.94+01.06 (green), and G192.60–00.04 (green and cyan). The spectroscopic properties of these detections are summarised in Table B.5, which includes source names, molecular line names, velocity-integrated intensities ($\int T_{mb} dv$), full-width at half-maximum (FWHM), and peak temperatures (T_{peak}) for all 31 regions. The velocity-integrated intensities of C_4H 9–8 transitions $J=19/2\text{-}17/2$ and $J=17/2\text{-}15/2$, exhibit a range of $0.11 \pm 0.03\ K\ km\ s^{-1}$ in G081.87+00.78 (green) to 1.25 ± 0.12 in G049.48–00.38 (cyan) and $0.13 \pm 0.04\ K\ km\ s^{-1}$ in G081.87+00.78 (green) to $1.33 \pm 0.10\ K\ km\ s^{-1}$ in G049.48–00.38 (cyan), respectively. By contrast, the $c\text{-}C_3H_2$ 2–1 were detected in G015.03–00.67 (green) with the strongest velocity-integrated fluxes of $6.42 \pm 0.06\ K\ km\ s^{-1}$, while the weakest emissions were found to be $0.98 \pm 0.06\ K\ km\ s^{-1}$ in G188.94+00.88 (green).

Under the assumptions of local thermodynamic equilibrium (LTE) and optical thinness, the column density of these

molecules can be calculated using the following formula,

$$N_{\text{tot}} = \frac{8\pi k\nu^2}{hc^3 A_{ul}} \frac{Q(T_{\text{ex}})}{g_u} e^{E_u/kT_{\text{ex}}} \int T_{\text{mb}} dv (\text{cm}^{-2}). \quad (1)$$

In the above equation, k represents the Boltzmann constant, ν is the frequency of the molecular emission line, h is the Planck constant, c is the speed of light, A_{ul} is the Einstein emission coefficient, g_u is the upper-level degeneracy, and E_u is the upper-level energy. The values for ν , g_u , A_{ul} , and E_u corresponding to the C₄H 9–8 ($J=19/2-17/2$), C₄H 9–8 ($J=19/2-19/2$), C₄H 9–8 ($J=17/2-15/2$), C₄H 9–8 ($J=17/2-17/2$), *c*-C₃H₂ 2–1, and H¹³CO⁺ 1–0 are shown in Table 1, which are taken from the CDMS database. The partition function $Q(T_{\text{ex}})$ predominantly depends on the excitation temperature T_{ex} . In this study a value of 37.5 K was adopted for T_{ex} , as all the sources were selected from hot cores.

The small difference in frequency between C₄H 9–8 ($J=19/2-17/2$) and C₄H 9–8 ($J=19/2-19/2$), as well as between C₄H 9–8 ($J=17/2-15/2$) and C₄H 9–8 ($J=17/2-17/2$) results in a blending of the lines, where only two emission features are observable across these four transitions. Therefore, based on Eq. 1, and considering the two blended lines with their respective values for A_{u1} , g_{u1} and A_{u2} , g_{u2} , the following equation can be derived to calculate the column density of C₄H,

$$N_{\text{tot}} = \frac{8\pi k\nu^2}{hc^3} \frac{Q(T_{\text{ex}})}{A_{u1}g_{u1} + A_{u2}g_{u2}} e^{E_u/kT_{\text{ex}}} \int T_{\text{mb}} dv (\text{cm}^{-2}). \quad (2)$$

Since the difference in E_u between the two blended molecular lines is also very small, we use the E_u values of C₄H 9–8 ($J=19/2-17/2$) and C₄H 9–8 ($J=17/2-15/2$) in Eq. 2. For sources with non-detection of C₄H 9–8 emission, 3σ upper limits for the integrated intensity, $\int T_{\text{mb}} dv$, were calculated using the formula $3 \times rms \sqrt{\delta\nu} \cdot \Delta\nu$, where $\delta\nu$ is the channel separation in velocity, $\Delta\nu$ is the velocity range for integration in km s⁻¹, and rms is the root mean square value per channel of the spectrum.

The column densities of C₄H, *c*-C₃H₂, and H¹³CO⁺ are displayed in columns 2–4 of Table B.6. The range of column densities for C₄H spans from 0.33×10^{13} cm⁻² in G081.87+00.78 (green) to 3.67×10^{13} cm⁻² in G049.48-00.38 (cyan), *c*-C₃H₂ range from 2.68×10^{13} cm⁻² in G188.94+00.88 (green) to 17.57×10^{13} cm⁻² in G015.03-00.67 (green), and H¹³CO⁺ from 0.48×10^{13} cm⁻² in G192.60-00.04 (cyan) to 4.92×10^{13} cm⁻² in G049.48-00.36 (green).

The relative abundances of the three molecules, which can be derived from the averaged column densities for each core, are more important than the averaged densities for the scientific analysis in this study. Table B.6 exhibits the abundance ratios [C₄H/H¹³CO⁺], [*c*-C₃H₂/H¹³CO⁺], and [C₄H/*c*-C₃H₂] in these 26 regions. The abundance ratio of [C₄H/H¹³CO⁺] ranges from 0.17 ± 0.04 in G081.87+00.78 (green) to 1.77 ± 0.11 in G049.48-00.38 (cyan), with a median value of 0.57, while it ranges from 1.42 ± 0.05 in G081.87+00.78 (green) to 6.69 ± 0.34 in G192.60-00.04 (cyan) with a median value of 4.19 for [*c*-C₃H₂/H¹³CO⁺]. For the ratio [C₄H/*c*-C₃H₂], the values range from 0.07 ± 0.01 in G081.75+00.59 (green) to 0.29 ± 0.03 in G133.94+01.06 (green), with a median value of 0.13. By combining data from 25 regions selected from 19 cold cores in a previous work (Liu et al. 2024) with current data from 26 regions of 22 hot cores, we obtained the relation between the abundances of C₄H and *c*-C₃H₂ normalised by H¹³CO⁺. It is shown in Fig. 2, with a Pearson correlation coefficient of 0.83, a slope of 3.41, and a least-squares fitting.

4. Discussion

4.1. Relative abundances of C₄H and *c*-C₃H₂ from cold and hot cores.

As shown in Fig. 2, the abundance ratios of C₄H and *c*-C₃H₂ relative to H¹³CO⁺ decreases from cold cores (Liu et al. 2024) to hot cores, suggesting a downward trend with advancing evolutionary stage of star formation. A least-squares fitting procedure results in the relation: $\lg(\text{C}_4\text{H}/\text{H}^{13}\text{CO}^+) = 3.41\lg(\text{c-C}_3\text{H}_2/\text{H}^{13}\text{CO}^+) - 3.20$, with a correlation coefficient of 0.83 (excluding C₄H upper limits). Among these 31 hot regions, column densities of both *c*-C₃H₂ and H¹³CO⁺ were successfully obtained, while C₄H was acquired for 18 regions. Specifically, C₄H/H¹³CO⁺ ratio ranges from 0.17 to 1.77 (median \sim 0.57), and *c*-C₃H₂/H¹³CO⁺ ratio spans 1.42 to 6.69 (median \sim 4.19) in hot cores, whereas cold cores exhibit significantly higher ratios of C₄H/H¹³CO⁺ (3–50) and *c*-C₃H₂/H¹³CO⁺ ratios (2–18) (Liu et al. 2024). This observational trend may be closely related to the low temperatures (10–20 K) that are characteristic of cold molecular cores. Given that these cloud cores typically form during the early phases of interstellar material accretion, their chemical evolution has not yet been significantly disrupted by star-forming activity (Aikawa et al. 2001; Sakai & Yamamoto 2013). Under such low-temperature conditions, the formation pathways of unsaturated hydrocarbons (C₄H and *c*-C₃H₂) gain a competitive advantage. The low-temperature environment favors simpler reaction mechanisms, particularly because reduced molecular collision rates allow such species to accumulate and sustain relatively high abundances within cold molecular cores (Loison et al. 2017). In contrast, massive star-forming regions exhibit higher temperatures (typically 30–100 K), where star formation activity is more mature. Under these conditions, intense radiation and physical conditions significantly alter the chemical environment of the molecular clouds. The high-temperature conditions may be expected to accelerate the consumption or conversion of these originally stable small molecules into more complex organic species, leading to reduced abundances of C₄H and *c*-C₃H₂ (Herbst & van Dishoeck 2009; Rodgers & Charnley 2003), which is also consistent with our observational results.

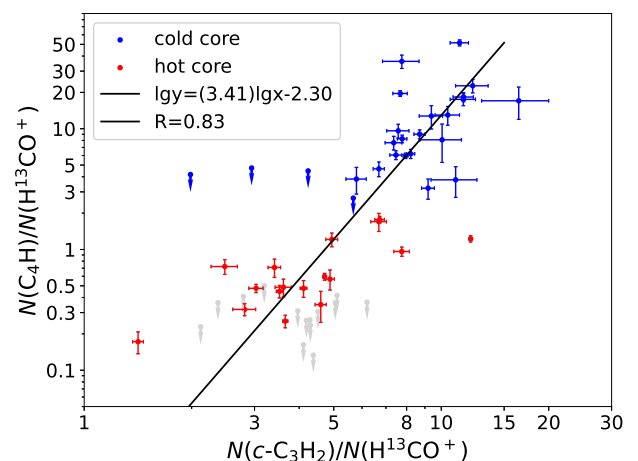


Fig. 2. Relation between *c*-C₃H₂/H¹³CO⁺ and C₄H/H¹³CO⁺ abundance ratios. Data are from 31 regions in 22 hot cores (red points) and 22 regions in 19 cold cores (blue points).

Additionally, it has been established that C₄H forms efficiently via gas-phase ion–molecule reactions, a process partic-

ularly effective at low temperatures during the early stages of star formation (Herbst & Osamura 2008). Fontani et al. (2025) investigated three sources at different evolutionary stages and found that both C_4H and $c\text{-}C_3H_2$ exhibit higher abundances in the earlier phases. It was concluded that C_4H is also formed through the reaction of C_2H_2 with C_2 , a process which was found to be more efficient at lower temperatures (Canosa et al. 2007). During the late stages of star formation, thermal processing leads to the desorption of molecules such as H_2O , CH_3OH , and O_2 from dust-grain ice mantles into the gas phase, where C_4H is rapidly consumed through reactions with these species (Herbst & Osamura 2008). The derived spatial distribution shows that the emission of C_4H 9–8 and $c\text{-}C_3H_2$ 2–1 is relatively weak across most regions near the excitation peak of $H42\alpha$. In sources such as G015.03-00.67, G049.48-00.36, G049.48-00.38, G075.76+00.33, and G035.19-01.73, the emission is primarily concentrated at the edge of $H42\alpha$. Additionally, in regions such as G012.80-00.20 and G043.16+00.01, C_4H 9–8 was not detected where the emission of $H^{13}CO^+$ 1–0 was strong. These positions exhibited $c\text{-}C_3H_2/H^{13}CO^+$ abundance ratios of 2.17 ± 0.14 and 2.05 ± 0.25 , respectively. This finding suggests that unsaturated molecules such as C_4H and $c\text{-}C_3H_2$ can be destroyed or processed into more complex organic molecules during the evolution of molecular cloud cores, leading to a corresponding decrease in their abundances.

4.2. Chemical models

We employed the NAUTILUS three-phase chemical model (Ruaud et al. 2016; Wakelam et al. 2024), which includes gas-phase, grain-surface, and grain-mantle chemistry, to simulate the chemical evolution of $c\text{-}C_3H_2$ and C_4H in both cold-core and hot-core environments. For the cold-core model, typical static physical conditions are adopted. The total hydrogen nuclei density is set to $n_H = 10^4 \text{ cm}^{-3}$, the temperature is fixed at $T = 10 \text{ K}$, and the cosmic-ray ionisation rate is taken to be $\zeta = 1.3 \times 10^{-17} \text{ s}^{-1}$. The hot-core physical model is divided into two successive stages: a free-fall collapse stage followed by a warm-up stage. During the collapse stage, the temperature remains constant at $T = 10 \text{ K}$, while the density increases from 3×10^3 to $3 \times 10^6 \text{ cm}^{-3}$. In the warm-up stage, the density is kept constant, and the temperature gradually increases up to 100 K .

The optically thin $H^{13}CO^+$ 1–0 isotopologue line was employed to normalise the relative abundances of $c\text{-}C_3H_2$ and C_4H relative to $H^{13}CO^+$ from their observed intensities. Figure 3 shows the abundances of $c\text{-}C_3H_2$, C_4H , and HCO^+ , as the major isotopic molecule of $H^{13}CO^+$, predicted by the models. The shaded regions indicate the observational abundance ranges of the corresponding species. Observations show that the abundance of C_4H and HCO^+ in cold cores is approximately two orders of magnitude higher than that in hot cores, while the abundance of $c\text{-}C_3H_2$ in cold cores is about one order of magnitude higher than that in hot cores. Figures 4 and 5 show the net percentage contributions of the formation and destruction pathways of $c\text{-}C_3H_2$ and C_4H , respectively, in cold and hot cores. Because the chemistry of these species involves a large number of reactions (e.g. more than 100 reactions for C_4H), only reaction pathways with contributions greater than 5% are shown in the figures. Reaction pathways for which the products are not explicitly labeled correspond to reactions with multiple product branching channels. Each panel shows the net percentage contributions of the formation or destruction pathways on the left-hand y-axis, while the abundances of $c\text{-}C_3H_2$ or C_4H are indicated on the right-hand y-axis.

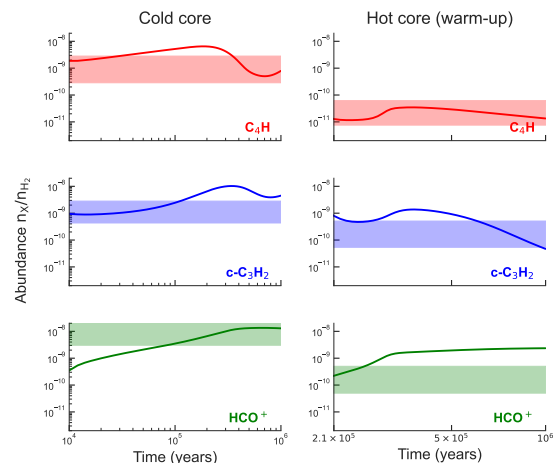


Fig. 3. Temporal evolution of $c\text{-}C_3H_2$, C_4H , and HCO^+ abundances predicted by models in cold core and hot core (warm-up).

According to the model results, in cold cores, $c\text{-}C_3H_2$ is mainly formed via the dissociative recombination of $C_3H_3^+$ with e^- , while C_4H is primarily produced through the dissociative recombination of $C_4H_2^+$ with e^- . During the collapse stage of the hot-core model, the formation pathways of $c\text{-}C_3H_2$ and C_4H are nearly identical to those in cold cores. However, as the density increases, both species are almost completely depleted toward the end of the collapse phase, with abundances falling below 10^{-12} . In the subsequent warm-up stage, $c\text{-}C_3H_2$ and C_4H are gradually reformed. Their formation pathways become more complex and differ significantly from those in cold cores. Meanwhile, the increasing temperature enhances their destruction efficiencies, which ultimately leads to lower abundances of both species in hot cores compared to cold cores. During the warm-up stage, $c\text{-}C_3H_2$ is mainly formed through the dissociative recombination of $C_3H_5^+$ with e^- , with an additional contribution from the dissociative recombination of $C_3H_3^+$. For C_4H , the dominant formation pathways include reactions involving HC_5NH^+ with e^- , as well as thermal desorption from grain surfaces as the temperature increases.

In both cold-core and hot-core environments, the destruction of $c\text{-}C_3H_2$ and C_4H is dominated by neutral–neutral reactions. In cold cores, however, the low temperatures significantly reduce the efficiency of neutral–neutral destruction pathways. As a result, the destruction rates are lower than the formation rates driven by dissociative recombination, allowing the abundances of $c\text{-}C_3H_2$ and C_4H to accumulate and reach higher levels than in hot cores.

In hot cores, the increasing gas density during the collapse stage and the rising temperature during the warm-up stage both enhance neutral–neutral destruction reactions. Consequently, the destruction of $c\text{-}C_3H_2$ and C_4H becomes more efficient, leading to lower abundances of these species compared to those in cold cores.

5. Summary and conclusions

We observed C_4H 9–8 lines, $c\text{-}C_3H_2$ 2–1, $H^{13}CO^+$ 1–0, and $H42\alpha$ toward 22 late-stage massive star-forming regions with the IRAM 30m telescope. Column densities and abundance ratios

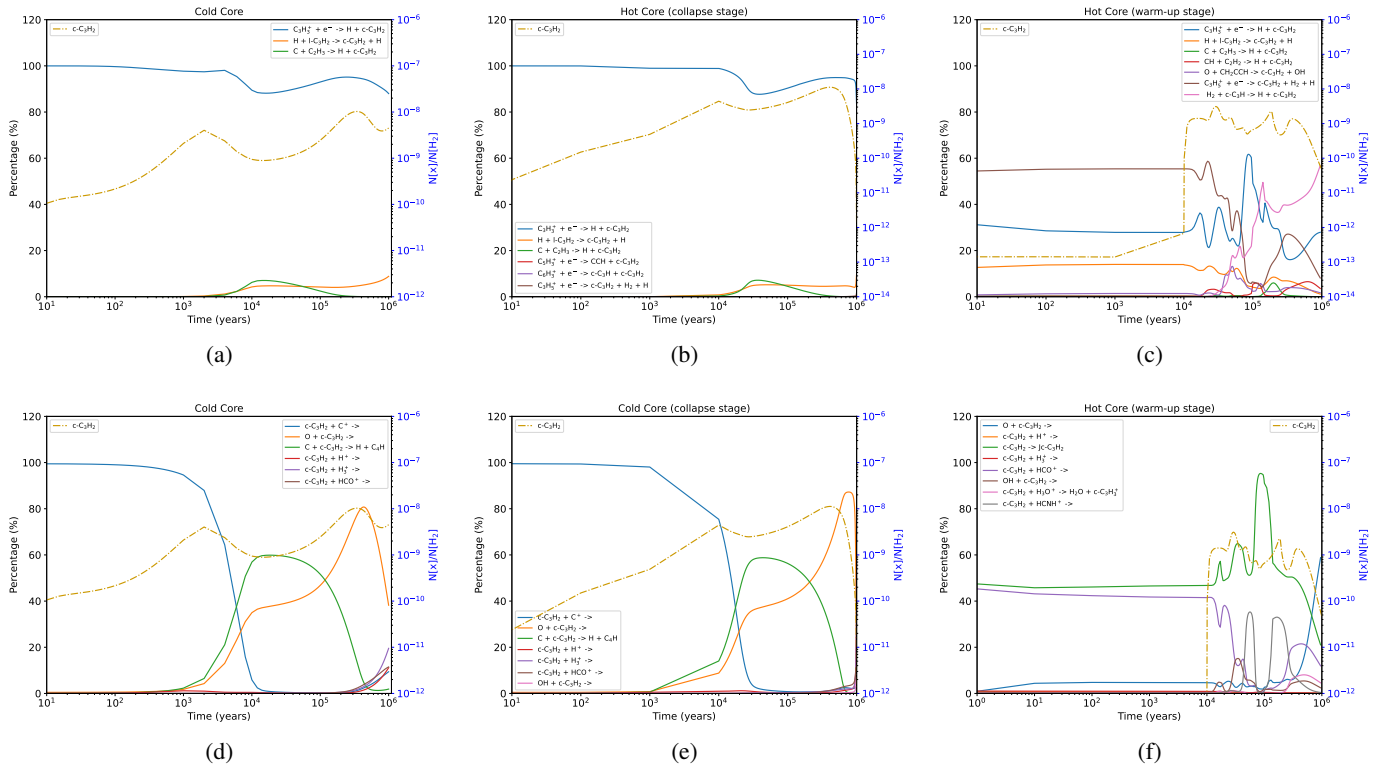


Fig. 4. Net percentage contributions of the formation and destruction pathways of $c\text{-}C_3H_2$ in cold and hot cores. (a) Net percentage contributions of the main formation pathways of $c\text{-}C_3H_2$ in cold molecular cloud cores. (b) Net percentage contributions of the main formation pathways of $c\text{-}C_3H_2$ during the hot-core collapse stage. (c) Net percentage contributions of the main formation pathways of $c\text{-}C_3H_2$ during the hot-core warm-up stage. (d) Net percentage contributions of the main destruction pathways of $c\text{-}C_3H_2$ in cold molecular cloud cores. (e) Net percentage contributions of the main destruction pathways of $c\text{-}C_3H_2$ during the hot-core collapse stage. (f) Net percentage contributions of the main destruction pathways of $c\text{-}C_3H_2$ during the hot-core warm-up stage.

were derived under local thermodynamic equilibrium, combined with data from 19 cold cores to explore evolutionary trends.

C_4H 9–8 lines were detected in 17 regions, specifically: G015.03–00.67 (green and cyan), G023.43–00.18 (green), G034.39+00.22 (green), G049.48–00.36 (green and cyan), G049.48–00.38 (green and cyan), G075.76+00.33 (green), G081.75+00.59–1 (green and cyan), G081.75+00.59–2 (green and cyan), G081.87+00.78 (green), G133.94+01.06 (green), and G192.60–00.04 (green and cyan), out of 31 regions toward 22 sources, while $c\text{-}C_3H_2$ 2–1 and $H^{13}CO^+$ 1–0 were detected in all regions. Both carbon-chain molecules are spatially concentrated at the edges of $H42\alpha$ emission regions, avoiding harsh HII region core environments. The abundance ratios in late-stage regions are: $C_4H/H^{13}CO^+$ (0.170–1.77, median \sim 0.57), $c\text{-}C_3H_2/H^{13}CO^+$ (1.42–6.69, median \sim 4.19), and $C_4H/c\text{-}C_3H_2$ (0.07–0.29, median \sim 0.13), all significantly lower than in cold cores.

NAUTILUS three-phase model simulations confirm this evolutionary trend, predicting higher abundances in cold cores by one to two orders of magnitude than in hot cores. Formation mechanisms shift from dissociative recombination (cold cores) to gas-phase reactions and grain desorption (late-stage regions), with destruction enhanced by neutral-neutral reactions in high-temperature and high-density environments.

Acknowledgements. This work is supported by National Key R&D Program of China under grant 2023YFA1608204, the National Natural Science Foundation of China grant 12550003 and the Guangxi Talent Programme (Highland of Innovation Talents). This work is based on observations carried out under project number 042-19, with the IRAM 30m telescope. N. Y.-T. acknowledges support from the National Natural Science Foundation of China

(grant Nos. 12473023), the University Annual Scientific Research Plan of Anhui Province (Nos. 2023AH030052). Y. L. acknowledges support from the Leading Innovation and Entrepreneurship Team of Zhejiang Province of China (grant No. 2023R01008) and the Key R&D Program of Zhejiang, China (grant No. 2024SSYS0012). D.H.-Q. acknowledges support from the National Key R&D program of China grant (2025YFE0108200) and the National Natural Science Foundation of China (No. 12373026). K.Y. acknowledges supports from the National Natural Science Foundation of China under Grant Number 12503031, the Postdoctoral Fellowship Program of CPSF under Grant Number GZC20252099, the Shanghai Post-doctoral Excellence Program (No. 2024379), the Natural Science Foundation of Shanghai (No. 25ZR1402267) and the Yangyang Development Fund. IRAM is supported by INSU/CNRS (France), MPG (Germany) and IGN (Spain).

References

- Awad, Z. & Viti, S. 2022, MNRAS, 511, 3, 3832. doi:10.1093/mnras/stac297
 Aikawa, Y., Ohashi, N., Inutsuka, S.-ichiro, et al. 2001, ApJ, 552, 2, 639. doi:10.1086/320551
 Canosa, A., Páramo, A., Le Picard, S. D., et al. 2007, Icarus, 187, 2, 558. doi:10.1016/j.icarus.2006.10.009
 Fontani, F., Rivilla, V. M., Roueff, E., et al. 2025, A&A, 700, A245. doi:10.1051/0004-6361/202555901
 Fossé, D., Cernicharo, J., Gerin, M., et al. 2001, ApJ, 552, 1, 168. doi:10.1086/320471
 Gianturco, F. A., Grassi, T., & Wester, R. 2016, Journal of Physics B Atomic Molecular Physics, 49, 204003. doi:10.1088/0953-4075/49/20/204003
 Ginsburg, A., Bressert, E., Bally, J., et al. 2012, ApJ, 758, 2, L29. doi:10.1088/2041-8205/758/2/L29
 Harada, N. & Herbst, E. 2008, ApJ, 685, 1, 272. doi:10.1086/590468
 Herbst, E. & van Dishoeck, E. F. 2009, ARA&A, 47, 1, 427. doi:10.1146/annurev-astro-082708-101654
 Herbst, E. & Osamura, Y. 2008, ApJ, 679, 2, 1670. doi:10.1086/587803
 Irvine, W. M., Hoglund, B., Friberg, P., et al. 1981, ApJ, 248, L113. doi:10.1086/183637

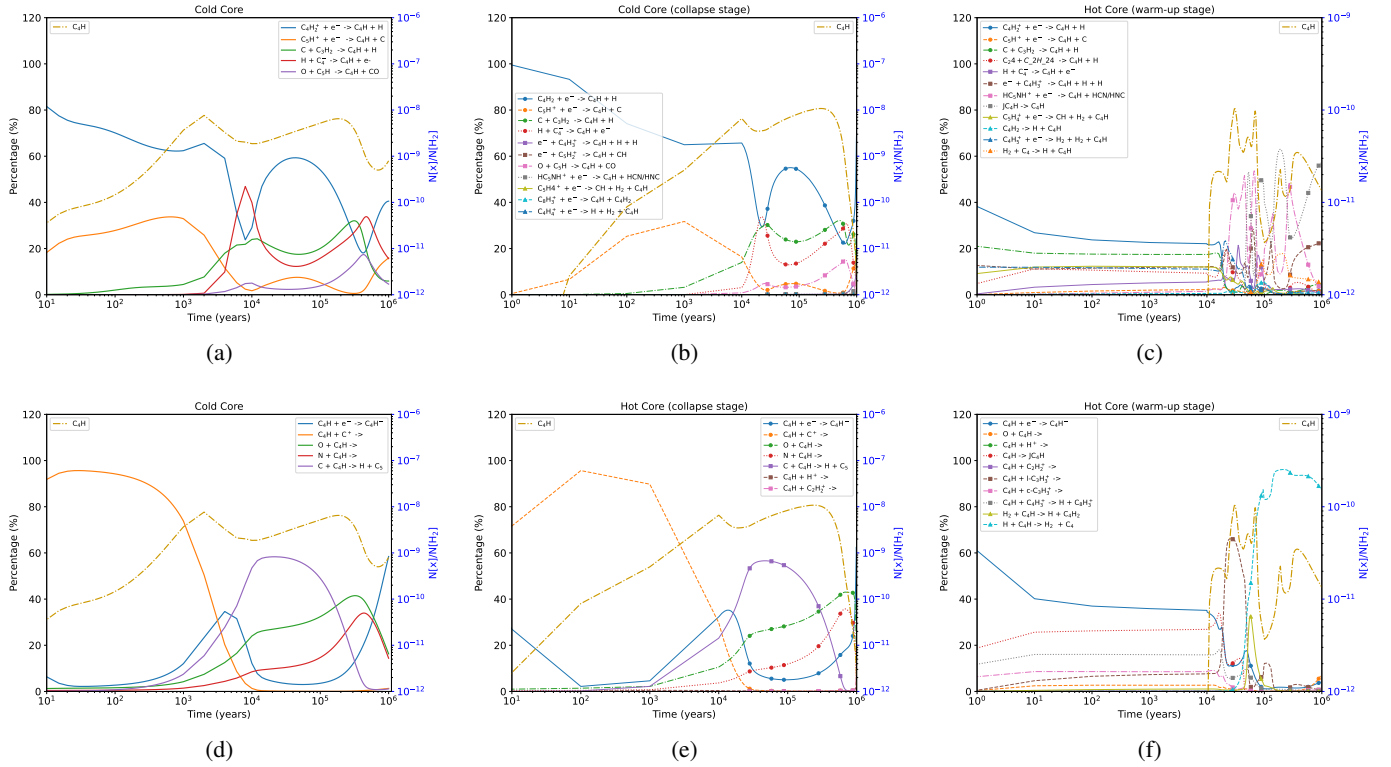


Fig. 5. Net percentage contributions of the formation and destruction pathways of C_4H in cold and hot cores. (a) Net percentage contributions of the main formation pathways of C_4H in cold molecular cloud cores. (b) Net percentage contributions of the main formation pathways of C_4H during the hot-core collapse stage. (c) Net percentage contributions of the main formation pathways of C_4H during the hot-core warm-up stage. (d) Net percentage contributions of the main destruction pathways of C_4H in cold molecular cloud cores. (e) Net percentage contributions of the main destruction pathways of C_4H during the hot-core collapse stage. (f) Net percentage contributions of the main destruction pathways of C_4H during the hot-core warm-up stage.

- Liu, Y., Wang, J., Liu, S., et al. 2024, *ApJ*, 969, 33. doi:10.3847/1538-4357/ad47a3
- Loison, J.-C., Wakelam, V., Hickson, K. M., et al. 2014, *MNRAS*, 437, 1, 930. doi:10.1093/mnras/stt1956
- Loison, J.-C., Agúndez, M., Wakelam, V., et al. 2017, *MNRAS*, 470, 4, 4075. doi:10.1093/mnras/stx1265
- Lucas, R. & Liszt, H. S. 2000, *A&A*, 358, 1069.
- Madden, S. C., Irvine, W. M., Matthews, H. E., et al. 1989, *AJ*, 97, 1403. doi:10.1086/115081
- Müller H. S. P., Schlöder F., Stutzki J., Winnewisser G., 2005, *JMoSt*, 742, 215. doi:10.1016/j.molstruc.2005.01.027
- Olano, C. A., Walmsley, C. M., & Wilson, T. L. 1988, *A&A*, 196, 194.
- Reid, M. J., Menten, K. M., Brunthaler, A., et al. 2014, *ApJ*, 783, 130. doi:10.1088/0004-637X/783/2/130
- Remijan, A., Scola, H. N., Burkhardt, A. M., et al. 2023, *ApJ*, 944, L45. doi:10.3847/2041-8213/acb648
- Rodgers, S. D. & Charnley, S. B. 2003, *ApJ*, 585, 1, 355. doi:10.1086/345497
- Ruud, M., Wakelam, V., & Hersant, F. 2016, *MNRAS*, 459, 4, 3756. doi:10.1093/mnras/stw88
- Sakai, N., Sakai, T., Hirota, T., et al. 2008, *ApJ*, 672, 1, 371. doi:10.1086/523635
- Sakai, N. & Yamamoto, S. 2013, *Chemical Reviews*, 113, 12, 8981. doi:10.1021/cr4001308
- Taniguchi, K., Gorai, P., Tan, J. C., et al. 2024, *A&A*, 692, A65. doi:10.1051/0004-6361/202451499
- Takakuwa, S., Ohashi, N., & Aikawa, Y. 2011, *ApJ*, 728, 2, 101. doi:10.1088/0004-637X/728/2/101
- Thaddeus, P., Vrtilik, J. M., & Gottlieb, C. A. 1985, *ApJ*, 299, L63. doi:10.1086/184581
- Wakelam, V., Gratier, P., Loison, J.-C., et al. 2024, *A&A*, 689, A63. doi:10.1051/0004-6361/202450606

Appendix A: The spatial distribution maps and spectral lines of all sources

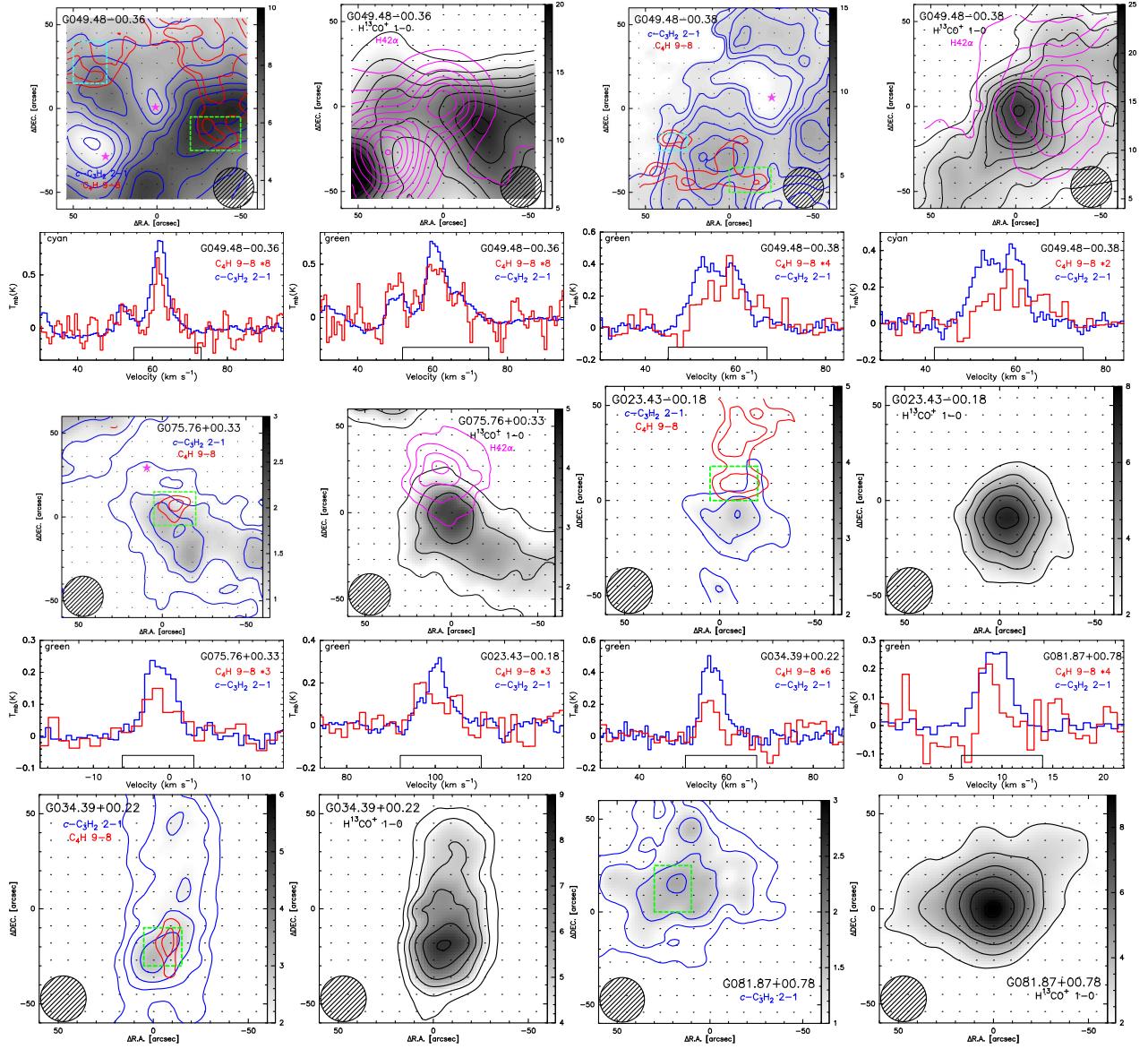


Fig. A.1. Same as Fig. 1 but for more sources.

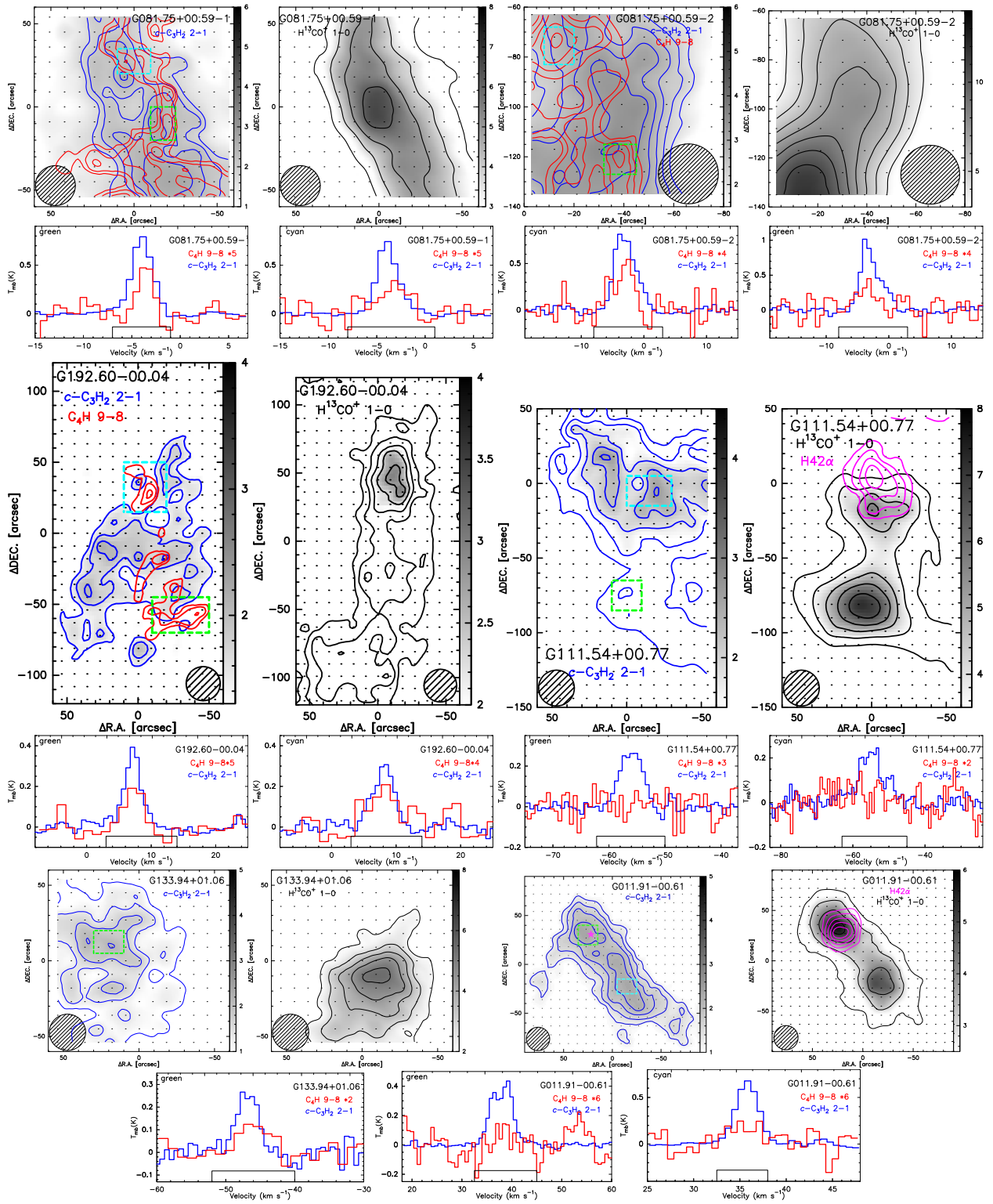


Fig. A.1. Continued.

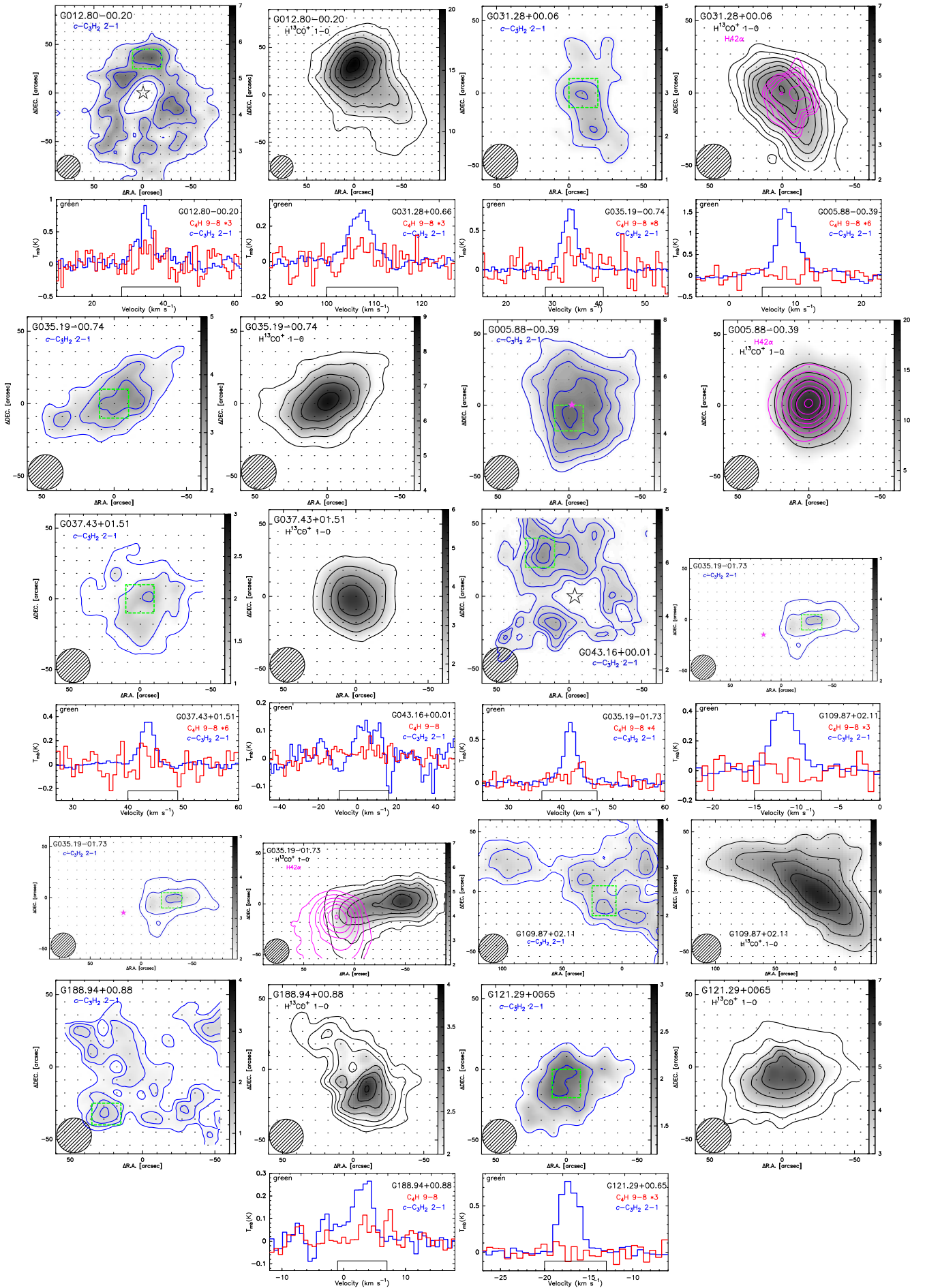


Fig. A.1. Continued.

Appendix B: Source information and observing parameters in hot cores

Table B.1. Source information and observing parameters in hot cores.

Source name Hot cores	RA (hh:mm:ss)	Decl. (dd:mm:ss)	rms (10^{-2} K)	Mapping size ($''$)	v_{LSR} (km s^{-1})
G005.88-00.39	18:00:30.31	-24:04:04.50	4.5	120 × 120	9.0
G011.91-00.61	18:13:59.72	-18:53:50.30	3.2	180 × 180	37.0
G012.80-00.20	18:14:14.23	-17:55:40.50	3.8	180 × 180	34.0
G015.03-00.67	18:20:22.01	-16:12:11.30	2.5	240 × 240	22.0
G023.43-00.18	18:34:39.29	-08:31:25.40	3.1	120 × 120	97.0
G031.28+00.06	18:48:12.39	-01:26:30.70	4.4	120 × 120	109.0
G034.39+00.22	18:53:19.00	+01:24:50.80	5.3	120 × 120	57.0
G035.19-00.74	18:58:13.05	+01:40:35.70	2.4	120 × 120	30.0
G035.19-01.73	19:01:45.54	+01:13:32.50	3.5	180 × 120	42.0
G037.43+01.51	18:54:14.35	+04:41:41.70	4.7	120 × 120	41.0
G043.16+00.01	19:10:13.41	+09:06:12.80	3.4	120 × 120	10.0
G049.48-00.36	19:23:39.82	+14:31:05.00	4.1	120 × 120	56.0
G049.48-00.38	19:23:43.87	+14:30:29.50	4.3	120 × 120	58.0
G075.76+00.33	20:21:41.09	+37:25:29.30	3.4	120 × 120	-9.0
G081.75+00.59	20:39:01.99	+42:24:59.30	2.7	120 × 180	-3.0
G081.87+00.78	20:38:36.43	+42:37:34.80	5.5	120 × 120	7.0
G109.87+02.11	22:56:18.10	+62:01:49.50	5.2	150 × 120	-7.0
G111.54+00.77	23:13:45.36	+61:28:10.60	3.7	120 × 200	-57.0
G121.29+00.65	00:36:47.35	+63:29:02.20	4.8	120 × 120	-23.0
G133.94+01.06	02:27:03.82	+61:52:25.20	4.6	120 × 120	-47.0
G188.94+00.88	06:08:53.35	+21:38:28.70	6.3	120 × 120	8.0
G192.60-00.04	06:12:54.02	+17:59:47.30	4.2	120 × 240	6.0

Table B.2. Spectral detection information of C_4H 9–8, $c\text{-C}_3\text{H}_2$ 2–1, and H^{13}CO^+ 1–0.

Source name	$\text{C}_4\text{H}(9-8)$	$c\text{-C}_3\text{H}_2(2-1)$	$\text{H}^{13}\text{CO}^+(1-0)$	Colour box
G005.88-00.39	...	✓	✓	green
G011.91-00.61	...	✓	✓	green
G011.91-00.61	...	✓	✓	cyan
G012.80-00.20	...	✓	✓	green
G015.03-00.67	✓	✓	✓	green
G015.03-00.67	✓	✓	✓	cyan
G023.43-00.18	✓	✓	✓	green
G031.28+00.66	...	✓	✓	green
G034.39+00.22	✓	✓	✓	green
G035.19-00.74	...	✓	✓	green
G035.19-01.73	...	✓	✓	green
G037.43+01.51	...	✓	✓	green
G043.16+00.01	...	✓	✓	green
G049.48-00.36	✓	✓	✓	green
G049.48-00.36	✓	✓	✓	cyan
G049.48-00.38	✓	✓	✓	green
G049.48-00.38	✓	✓	✓	cyan
G075.76+00.33	✓	✓	✓	green
G081.75+00.59-1	✓	✓	✓	green
G081.75+00.59-1	✓	✓	✓	cyan
G081.75+00.59-2	✓	✓	✓	green
G081.75+00.59-2	✓	✓	✓	cyan
G081.87+00.78	✓	✓	✓	green
G109.87+02.11	...	✓	✓	green
G111.54+00.77	...	✓	✓	green
G111.54+00.77	...	✓	✓	cyan
G121.29+00.65	...	✓	✓	green
G133.94+01.06	✓	✓	✓	green
G188.94+00.88	...	✓	✓	green
G192.60-00.04	✓	✓	✓	green
G192.60-00.04	✓	✓	✓	cyan

Table B.3. Information parameters for the map setting of C₄H 9–8, *c*-C₃H₂ 2–1, and H¹³CO⁺ 1–0 in hot cores.

Source name	C ₄ H(9-8)			<i>c</i> -C ₃ H ₂ (2-1)			H ¹³ CO ⁺ (1-0)			H42 α		
	1 σ	starting	step	1 σ	starting	step	1 σ	starting	step	1 σ	starting	step
	K km s ⁻¹	K km s ⁻¹	K km s ⁻¹	K km s ⁻¹	K km s ⁻¹	K km s ⁻¹	K km s ⁻¹	K km s ⁻¹	K km s ⁻¹	K km s ⁻¹	K km s ⁻¹	K km s ⁻¹
G005.88-00.39	0.06	0.15	3.8	2.0	0.2	6.0	3.0	0.25	4.0	5.0
G011.91-00.61	0.06	0.10	2.5	0.55	0.17	1.8	1.2	0.2	1.8	0.8
G012.80-00.20	0.07	0.17	4.5	2.0	0.15	4.0	2.5
G015.03-00.67	0.26	1.4	0.3	0.20	4.0	2.0	0.22	4.0	3.0	0.25	5.0	3.0
G023.43-00.18	0.22	0.5	0.2	0.18	1.5	0.8	0.15	2.0	1.2
G031.28+00.06	0.045	0.16	1.8	0.8	0.13	1.2	0.5	0.12	0.5	0.2
G034.39+00.22	0.21	0.7	0.2	0.32	3.2	0.8	0.21	3.0	1.0
G035.19-00.74	0.06	0.16	3.3	1.2	0.24	3.3	1.2
G035.19-01.73	0.05	0.13	1.3	0.8	0.15	1.3	0.8	0.25	3.5	2.2
G037.43+01.51	0.053	0.13	1.5	0.9	0.13	1.5	0.9
G043.16+00.01	0.05	0.48	3.0	1.5	0.22	3.2	1.2
G049.48-00.36	0.23	0.8	0.3	0.24	4.0	2.3	0.24	4.0	2.3	0.21	4.0	2.0
G049.48-00.38	0.25	0.8	0.3	0.46	4.0	2.3	0.24	4.0	2.3	0.21	4.0	2.0
G075.76+00.33	0.09	0.3	0.1	0.25	1.9	0.8	0.15	1.2	1.0	0.17	2.0	1.0
G081.75+00.59-1	0.06	0.22	2.4	1.2	0.23	2.5	1.2
G081.75+00.59-2	0.16	0.8	0.2	0.18	3.2	0.8	0.19	3.2	1.2
G081.87+00.78	0.16	2	0.3	0.18	2.7	1.0	0.15	2.2	1.3
G109.87+02.11	0.06	0.22	3.2	1.2	0.28	3.5	1.2
G111.54+00.77	0.06	0.17	2.5	1.0	0.16	2.5	1.0	0.12	1.2	0.8
G121.29+00.65	0.04	0.25	2.5	0.8	0.15	1.8	0.8
G133.94+01.06	0.24	0.8	0.2	0.13	2.0	0.7	0.21	2.0	0.8
G188.94+00.88	0.05	0.25	1.8	0.5	0.15	1.2	0.4
G192.60-00.04	0.20	0.65	0.15	0.17	1.0	0.6	0.12	0.8	0.5

Table B.4. Distribution information of C₄H 9–8, *c*-C₃H₂ 2–1, and H¹³CO⁺ 1–0.

Source Name	C ₄ H(9-8)		<i>c</i> -C ₃ H ₂ (2-1)		Difference between C ₄ H(9-8) and <i>c</i> -C ₃ H ₂ (2-1)
	Detection	Clear feature	Detection	Clear feature	
G005.88-00.39	✓	✓	...
G011.91-00.61	✓	✓	...
G012.80-00.20	✓	✓	...
G015.03-00.67	✓	✓	✓	✓	✓
G023.43-00.18	✓	✓	✓	✓	✓
G031.28+00.66	✓	✓	...
G034.39+00.22	✓	...	✓	✓	...
G035.19-00.74	✓	✓	...
G035.19-01.73	✓	✓	...
G037.43+01.51	✓	✓	...
G043.16+00.01	✓	✓	...
G049.48-00.36	✓	✓	✓	✓	✓
G049.48-00.38	✓	✓	✓	✓	✓
G075.76+00.33	✓	...	✓	✓	...
G081.75+00.59	✓	✓	✓	✓	✓
G081.87+00.78	✓	✓	...
G109.87+02.11	✓	✓	...
G111.54+00.77	✓	✓	...
G121.29+00.65	✓	✓	...
G133.94+01.06	✓	✓	...
G188.94+00.88	✓	✓	...
G192.60-00.04	✓	✓	✓	✓	✓

Table B.5. Observed data for the C₄H, c-C₃H₂, and H¹³CO⁺ lines.

Source name	Molecular line	$\int T_{\text{mb}} dv$ (K km s ⁻¹)	FWHM (km s ⁻¹)	T_{peak} (K)	Box colour
G005.88-00.39	C ₄ H N=9-8 J=19/2-17/2	≤ 0.18	green
	C ₄ H N=9-8 J=17/2-15/2	≤ 0.22	
	c-C ₃ H ₂ J=2(1,2)-1(0,1)	5.65 ± 0.09	3.49 ± 0.06	1.52	
	H ¹³ CO ⁺ J=1-0	13.60 ± 0.19	3.92 ± 0.07	3.26	
G011.91-00.61	C ₄ H N=9-8 J=19/2-17/2	≤ 0.15	green
	C ₄ H N=9-8 J=17/2-15/2	≤ 0.18	
	c-C ₃ H ₂ J=2(1,2)-1(0,1)	2.14 ± 0.04	5.26 ± 0.10	0.38	
	H ¹³ CO ⁺ J=1-0	5.00 ± 0.04	4.59 ± 0.04	1.02	
G011.91-00.61	C ₄ H N=9-8 J=19/2-17/2	≤ 0.16	cyan
	C ₄ H N=9-8 J=17/2-15/2	≤ 0.16	
	c-C ₃ H ₂ J=2(1,2)-1(0,1)	1.96 ± 0.05	2.79 ± 0.08	0.66	
	H ¹³ CO ⁺ J=1-0	4.05 ± 0.06	3.84 ± 0.07	0.99	
G012.80-00.20	C ₄ H N=9-8 J=19/2-17/2	≤ 0.23	green
	C ₄ H N=9-8 J=17/2-15/2	≤ 0.21	
	c-C ₃ H ₂ J=2(1,2)-1(0,1)	3.87 ± 0.37	5.01 ± 0.67	0.73	
	H ¹³ CO ⁺ J=1-0	6.59 ± 0.12	4.81 ± 0.10	1.29	
G015.03-00.67	C ₄ H N=9-8 J=19/2-17/2	0.83 ± 0.08	5.38 ± 0.60	0.15	green
	C ₄ H N=9-8 J=17/2-15/2	0.74 ± 0.06	4.54 ± 0.42	0.15	
	c-C ₃ H ₂ J=2(1,2)-1(0,1)	6.42 ± 0.06	5.10 ± 0.05	1.18	
	H ¹³ CO ⁺ J=1-0	14.37 ± 0.11	3.35 ± 0.03	4.03	
G015.03-0067	C ₄ H N=9-8 J=19/2-17/2	0.74 ± 0.05	4.86 ± 0.42	0.14	cyan
	C ₄ H N=9-8 J=17/2-15/2	0.43 ± 0.05	3.46 ± 0.47	0.12	
	c-C ₃ H ₂ J=2(1,2)-1(0,1)	5.89 ± 0.05	4.34 ± 0.05	1.28	
	H ¹³ CO ⁺ J=1-0	5.14 ± 0.04	3.14 ± 0.03	1.54	
G023.43-00.18	C ₄ H N=9-8 J=19/2-17/2	0.29 ± 0.07	9.00 ± 1.31	0.05	green
	C ₄ H N=9-8 J=17/2-15/2	0.25 ± 0.06	8.89 ± 1.12	0.05	
	c-C ₃ H ₂ J=2(1,2)-1(0,1)	2.08 ± 0.11	6.85 ± 0.45	0.29	
	H ¹³ CO ⁺ J=1-0	6.07 ± 0.06	4.91 ± 0.06	1.16	
G031.28+00.66	C ₄ H N=9-8 J=19/2-17/2	≤ 0.13	green
	C ₄ H N=9-8 J=17/2-15/2	≤ 0.16	
	c-C ₃ H ₂ J=2(1,2)-1(0,1)	1.63 ± 0.06	5.48 ± 0.24	0.28	
	H ¹³ CO ⁺ J=1-0	4.33 ± 0.04	4.30 ± 0.04	0.95	
G034.39+00.22	C ₄ H N=9-8 J=19/2-17/2	0.24 ± 0.08	10.20 ± 1.42	0.05	green
	C ₄ H N=9-8 J=17/2-15/2	0.22 ± 0.11	9.35 ± 2.02	0.04	
	c-C ₃ H ₂ J=2(1,2)-1(0,1)	3.17 ± 0.10	5.89 ± 0.23	0.51	
	H ¹³ CO ⁺ J=1-0	7.27 ± 0.11	4.61 ± 0.08	1.48	
G035.19-00.74	C ₄ H N=9-8 J=19/2-17/2	≤ 0.18	green
	C ₄ H N=9-8 J=17/2-15/2	≤ 0.17	
	c-C ₃ H ₂ J=2(1,2)-1(0,1)	2.88 ± 0.04	3.49 ± 0.06	0.77	
	H ¹³ CO ⁺ J=1-0	7.23 ± 0.06	4.33 ± 0.04	1.57	
G035.19-01.73	C ₄ H N=9-8 J=19/2-17/2	≤ 0.13	green
	C ₄ H N=9-8 J=17/2-15/2	≤ 0.15	
	c-C ₃ H ₂ J=2(1,2)-1(0,1)	2.06 ± 0.06	2.85 ± 0.11	0.68	
	H ¹³ CO ⁺ J=1-0	5.05 ± 0.05	2.46 ± 0.03	1.93	
G037.43+01.51	C ₄ H N=9-8 J=19/2-17/2	≤ 0.16	green
	C ₄ H N=9-8 J=17/2-15/2	≤ 0.14	
	c-C ₃ H ₂ J=2(1,2)-1(0,1)	1.09 ± 0.04	2.80 ± 0.11	0.37	
	H ¹³ CO ⁺ J=1-0	4.10 ± 0.05	2.56 ± 0.04	1.51	
G043.16+00.01	C ₄ H N=9-8 J=19/2-17/2	≤ 0.14	green
	C ₄ H N=9-8 J=17/2-15/2	≤ 0.13	
	c-C ₃ H ₂ J=2(1,2)-1(0,1)	3.46 ± 0.241	10.32 ± 0.56	0.20	
	H ¹³ CO ⁺ J=1-0	8.87 ± 0.15	13.29 ± 0.24	0.63	
G049.48-00.36	C ₄ H N=9-8 J=19/2-17/2	0.60 ± 0.09	12.21 ± 2.43	0.05	green
	C ₄ H N=9-8 J=17/2-15/2	0.51 ± 0.09	12.77 ± 3.52	0.04	
	c-C ₃ H ₂ J=2(1,2)-1(0,1)	5.06 ± 0.37	7.67 ± 0.85	0.62	
	H ¹³ CO ⁺ J=1-0	18.96 ± 0.06	7.88 ± 0.03	2.26	
G049.48-00.36	C ₄ H N=9-8 J=19/2-17/2	0.37 ± 0.06	3.00 ± 0.66	0.12	cyan
	C ₄ H N=9-8 J=17/2-15/2	0.57 ± 0.06	5.29 ± 0.62	0.10	
	c-C ₃ H ₂ J=2(1,2)-1(0,1)	3.96 ± 0.19	4.61 ± 0.27	0.81	
	H ¹³ CO ⁺ J=1-0	5.39 ± 0.09	3.75 ± 0.08	1.35	
G049.48-00.38	C ₄ H N=9-8 J=19/2-17/2	0.72 ± 0.11	11.51 ± 1.59	0.07	green
	C ₄ H N=9-8 J=17/2-15/2	0.72 ± 0.04	11.03 ± 0.94	0.07	
	c-C ₃ H ₂ J=2(1,2)-1(0,1)	4.73 ± 0.22	11.15 ± 0.52	0.40	
	H ¹³ CO ⁺ J=1-0	16.44 ± 0.08	7.72 ± 0.04	2.00	
G049.48-00.38	C ₄ H N=9-8 J=19/2-17/2	1.25 ± 0.12	13.14 ± 1.27	0.09	cyan

Table B.5. Continued.

Source name	Molecular Line	$\int T_{\text{mb}} dv$ (K·km s ⁻¹)	FWHM (km s ⁻¹)	T_{peak} (K)	Box colour	
G075.76+00.33	C ₄ H	N=9-8 J=17/2-15/2	1.33 ± 0.10	13.56 ± 1.11	0.09	green
	<i>c</i> -C ₃ H ₂	J=2(1,2)-1(0,1)	5.10 ± 0.12	11.84 ± 0.29	0.40	
	H ¹³ CO ⁺	J=1-0	7.99 ± 0.16	12.61 ± 0.28	0.60	
	C ₄ H	N=9-8 J=19/2-17/2	0.25 ± 0.05	5.17 ± 1.49	0.05	
G081.75+00.59-1	C ₄ H	N=9-8 J=17/2-15/2	0.20 ± 0.05	3.77 ± 1.25	0.05	green
	<i>c</i> -C ₃ H ₂	J=2(1,2)-1(0,1)	1.11 ± 0.04	4.32 ± 0.18	0.24	
	H ¹³ CO ⁺	J=1-0	3.42 ± 0.05	3.85 ± 0.07	0.83	
	C ₄ H	N=9-8 J=19/2-17/2	0.18 ± 0.03	1.60 ± 0.25	0.11	
G081.75+00.59-1	C ₄ H	N=9-8 J=17/2-15/2	0.10 ± 0.02	2.15 ± 0.29	0.07	cyan
	<i>c</i> -C ₃ H ₂	J=2(1,2)-1(0,1)	2.10 ± 0.03	2.51 ± 0.05	0.79	
	H ¹³ CO ⁺	J=1-0	6.06 ± 0.03	2.19 ± 0.01	2.60	
	C ₄ H	N=9-8 J=19/2-17/2	0.27 ± 0.06	4.20 ± 1.17	0.06	
G081.75+00.59-2	C ₄ H	N=9-8 J=17/2-15/2	0.18 ± 0.04	4.91 ± 1.05	0.03	green
	<i>c</i> -C ₃ H ₂	J=2(1,2)-1(0,1)	2.00 ± 0.04	2.58 ± 0.05	0.73	
	H ¹³ CO ⁺	J=1-0	5.11 ± 0.06	2.37 ± 0.03	2.03	
	C ₄ H	N=9-8 J=19/2-17/2	0.32 ± 0.09	3.52 ± 1.12	0.09	
G081.75+00.59 -2	C ₄ H	N=9-8 J=17/2-15/2	0.46 ± 0.12	4.73 ± 1.47	0.09	cyan
	<i>c</i> -C ₃ H ₂	J=2(1,2)-1(0,1)	3.49 ± 0.09	3.73 ± 0.12	0.88	
	H ¹³ CO ⁺	J=1-0	7.54 ± 0.10	4.14 ± 0.06	1.71	
	C ₄ H	N=9-8 J=19/2-17/2	0.51 ± 0.08	3.96 ± 0.69	0.12	
G081.87+00.78	C ₄ H	N=9-8 J=17/2-15/2	0.36 ± 0.07	3.21 ± 0.70	0.10	green
	<i>c</i> -C ₃ H ₂	J=2(1,2)-1(0,1)	3.46 ± 0.07	3.99 ± 0.09	0.82	
	H ¹³ CO ⁺	J=1-0	10.37 ± 0.06	4.26 ± 0.03	2.28	
	C ₄ H	N=9-8 J=19/2-17/2	0.11 ± 0.03	1.59 ± 0.41	0.06	
G109.87+02.11	C ₄ H	N=9-8 J=17/2-15/2	0.13 ± 0.04	1.60 ± 0.32	0.06	green
	<i>c</i> -C ₃ H ₂	J=2(1,2)-1(0,1)	0.99 ± 0.03	3.37 ± 0.13	0.28	
	H ¹³ CO ⁺	J=1-0	7.34 ± 0.06	3.95 ± 0.04	1.75	
	C ₄ H	N=9-8 J=19/2-17/2	≤ 0.16	
G111.54+00.77	C ₄ H	N=9-8 J=17/2-15/2	≤ 0.19	green
	<i>c</i> -C ₃ H ₂	J=2(1,2)-1(0,1)	1.44 ± 0.06	3.77 ± 0.17	0.36	
	H ¹³ CO ⁺	J=1-0	7.17 ± 0.08	3.44 ± 0.04	1.96	
	C ₄ H	N=9-8 J=19/2-17/2	≤ 0.21	
G111.54+00.77	C ₄ H	N=9-8 J=17/2-15/2	≤ 0.20	cyan
	<i>c</i> -C ₃ H ₂	J=2(1,2)-1(0,1)	1.37 ± 0.06	4.56 ± 0.20	0.28	
	H ¹³ CO ⁺	J=1-0	6.09 ± 0.05	4.35 ± 0.05	1.31	
	C ₄ H	N=9-8 J=19/2-17/2	≤ 0.15	
G121.29+00.65	C ₄ H	N=9-8 J=17/2-15/2	≤ 0.17	green
	<i>c</i> -C ₃ H ₂	J=2(1,2)-1(0,1)	1.98 ± 0.09	8.70 ± 0.52	0.21	
	H ¹³ CO ⁺	J=1-0	4.14 ± 0.07	3.77 ± 0.08	1.03	
	C ₄ H	N=9-8 J=19/2-17/2	≤ 0.12	
G133.94+01.06	C ₄ H	N=9-8 J=17/2-15/2	≤ 0.13	green
	<i>c</i> -C ₃ H ₂	J=2(1,2)-1(0,1)	2.11 ± 0.06	2.54 ± 0.08	0.78	
	H ¹³ CO ⁺	J=1-0	5.18 ± 0.04	2.46 ± 0.02	1.98	
	C ₄ H	N=9-8 J=19/2-17/2	0.34 ± 0.07	4.56 ± 1.03	0.07	
G188.94+00.88	C ₄ H	N=9-8 J=17/2-15/2	0.25 ± 0.04	1.14 ± 0.59	0.06	green
	<i>c</i> -C ₃ H ₂	J=2(1,2)-1(0,1)	1.05 ± 0.09	3.62 ± 0.34	0.27	
	H ¹³ CO ⁺	J=1-0	4.45 ± 0.08	3.40 ± 0.07	1.23	
	C ₄ H	N=9-8 J=19/2-17/2	≤ 0.16	
G192.60-00.04	C ₄ H	N=9-8 J=17/2-15/2	≤ 0.15	green
	<i>c</i> -C ₃ H ₂	J=2(1,2)-1(0,1)	0.98 ± 0.12	3.67 ± 0.54	0.25	
	H ¹³ CO ⁺	J=1-0	3.23 ± 0.08	3.03 ± 0.10	1.00	
	C ₄ H	N=9-8 J=19/2-17/2	0.18 ± 0.04	2.10 ± 0.61	0.07	
G192.60-00.04	C ₄ H	N=9-8 J=17/2-15/2	0.37 ± 0.06	6.52 ± 0.85	0.06	cyan
	<i>c</i> -C ₃ H ₂	J=2(1,2)-1(0,1)	1.19 ± 0.04	3.01 ± 0.12	0.37	
	H ¹³ CO ⁺	J=1-0	2.54 ± 0.05	2.81 ± 0.07	0.85	
	C ₄ H	N=9-8 J=19/2-17/2	0.25 ± 0.06	5.31 ± 1.69	0.04	
G192.60-00.04	C ₄ H	N=9-8 J=17/2-15/2	0.33 ± 0.07	8.60 ± 1.35	0.06	cyan
	<i>c</i> -C ₃ H ₂	J=2(1,2)-1(0,1)	1.18 ± 0.05	3.76 ± 0.19	0.30	
	H ¹³ CO ⁺	J=1-0	1.87 ± 0.04	2.96 ± 0.08	0.59	

Table B.6. Column density & relative abundance of C₄H, c-C₃H₂ and H¹³CO⁺.

Source name	$N(\text{C}_4\text{H})$ 10^{13}cm^{-2}	$N(\text{c-C}_3\text{H}_2)$ 10^{13}cm^{-2}	$N(\text{H}^{13}\text{CO}^+)$ 10^{13}cm^{-2}	$\frac{N_{\text{C}_4\text{H}}}{N_{\text{H}^{13}\text{CO}^+}}$	$\frac{N_{\text{c-C}_3\text{H}_2}}{N_{\text{H}^{13}\text{CO}^+}}$	$\frac{N_{\text{C}_4\text{H}}}{N_{\text{c-C}_3\text{H}_2}}$	Box colour
G005.88-00.39	≤ 0.73	15.47 ± 0.24	3.53 ± 0.05	≤ 0.13	4.38 ± 0.09	≤ 0.18	green
G011.91-00.61	≤ 0.61	5.86 ± 0.11	1.30 ± 0.01	≤ 0.31	4.52 ± 0.09	≤ 0.15	green
G011.91-00.61	≤ 0.79	5.36 ± 0.13	1.05 ± 0.02	≤ 0.42	5.11 ± 0.15	≤ 0.16	cyan
G012.80-00.20	≤ 1.16	10.60 ± 1.00	1.71 ± 0.03	≤ 0.37	6.20 ± 0.60	≤ 0.23	green
G015.03-00.67	2.22 ± 0.14	17.57 ± 0.16	2.73 ± 0.02	0.60 ± 0.04	4.71 ± 0.06	0.13 ± 0.01	green
G015.03-00.67	1.64 ± 0.10	16.12 ± 0.15	1.33 ± 0.01	1.23 ± 0.07	12.09 ± 0.14	0.10 ± 0.01	cyan
G023.43-00.18	0.77 ± 0.13	5.69 ± 0.29	1.57 ± 0.02	0.49 ± 0.08	3.61 ± 0.19	0.13 ± 0.02	green
G031.28+00.66	≤ 1.15	4.45 ± 0.17	1.12 ± 0.01	≤ 0.31	3.96 ± 0.16	≤ 0.13	green
G034.39+00.22	0.65 ± 0.19	8.67 ± 0.28	1.89 ± 0.03	0.35 ± 0.10	4.60 ± 0.17	0.08 ± 0.02	green
G035.19-00.74	≤ 0.69	7.87 ± 0.11	1.88 ± 0.02	≤ 0.26	4.19 ± 0.07	≤ 0.18	green
G035.19-01.73	≤ 0.88	5.62 ± 0.17	1.31 ± 0.01	≤ 0.26	4.29 ± 0.13	≤ 0.13	green
G037.43+01.51	≤ 0.43	2.97 ± 0.10	1.06 ± 0.01	≤ 0.41	2.79 ± 0.10	≤ 0.16	green
G043.16+00.01	≤ 1.87	9.43 ± 0.65	2.30 ± 0.04	≤ 0.16	4.11 ± 0.29	≤ 0.14	green
G049.48-00.36	1.57 ± 0.18	13.85 ± 0.10	4.92 ± 0.02	0.32 ± 0.04	2.81 ± 0.21	0.11 ± 0.02	green
G049.48-00.36	1.34 ± 0.12	10.84 ± 0.51	1.40 ± 0.02	0.96 ± 0.08	7.75 ± 0.39	0.12 ± 0.01	cyan
G049.48-00.38	2.03 ± 0.16	12.93 ± 0.59	4.26 ± 0.02	0.48 ± 0.04	3.03 ± 0.14	0.16 ± 0.01	green
G049.48-00.38	3.67 ± 0.22	13.94 ± 0.33	2.07 ± 0.04	1.77 ± 0.11	6.72 ± 0.21	0.26 ± 0.02	cyan
G075.76+00.33	0.62 ± 0.11	3.02 ± 0.11	0.89 ± 0.01	0.71 ± 0.12	3.41 ± 0.14	0.21 ± 0.04	green
G081.75+00.59-1	0.40 ± 0.05	5.75 ± 0.09	1.57 ± 0.01	0.25 ± 0.03	3.66 ± 0.06	0.07 ± 0.01	green
G081.75+00.59-1	0.63 ± 0.10	5.46 ± 0.10	1.33 ± 0.02	0.48 ± 0.08	4.12 ± 0.09	0.12 ± 0.02	cyan
G081.75+00.59-2	1.11 ± 0.21	9.55 ± 0.24	1.96 ± 0.03	0.57 ± 0.11	4.88 ± 0.14	0.12 ± 0.02	green
G081.75+00.59-2	1.21 ± 0.14	9.48 ± 0.19	2.69 ± 0.02	0.45 ± 0.05	3.52 ± 0.07	0.13 ± 0.02	cyan
G081.87+00.78	0.33 ± 0.07	2.70 ± 0.09	1.90 ± 0.02	0.17 ± 0.04	1.42 ± 0.05	0.12 ± 0.03	green
G109.87+02.11	≤ 0.98	3.94 ± 0.16	1.86 ± 0.02	≤ 0.23	2.12 ± 0.09	≤ 0.16	green
G111.54+00.77	≤ 0.71	3.75 ± 0.16	1.58 ± 0.01	≤ 0.36	2.37 ± 0.10	≤ 0.21	green
G111.54+00.77	≤ 2.66	5.43 ± 0.26	1.08 ± 0.02	≤ 0.36	5.05 ± 0.25	≤ 0.15	cyan
G121.29+00.65	≤ 0.64	5.78 ± 0.16	1.34 ± 0.01	≤ 0.24	4.30 ± 0.12	≤ 0.12	green
G133.94+01.06	0.83 ± 0.12	2.86 ± 0.24	1.16 ± 0.02	0.72 ± 0.10	2.48 ± 0.21	0.29 ± 0.05	green
G188.94+00.88	≤ 1.26	2.68 ± 0.31	0.84 ± 0.02	≤ 0.50	3.19 ± 0.39	≤ 0.16	green
G192.60-00.04	0.80 ± 0.11	3.25 ± 0.10	0.66 ± 0.01	1.29 ± 0.16	4.94 ± 0.19	0.25 ± 0.03	green
G192.60-00.04	0.83 ± 0.14	3.24 ± 0.15	0.48 ± 0.01	1.70 ± 0.29	6.69 ± 0.34	0.25 ± 0.04	cyan